

## Phase-sensitive evidence for $2\times 2$ pair density wave in a kagome superconductor

**Authors:** Xiao-Yu Yan<sup>1\*</sup>, Guowei Liu<sup>1\*</sup>, Hanbin Deng<sup>1\*</sup>, Xitong Xu<sup>2\*</sup>, Haiyang Ma<sup>3\*</sup>, Hailang Qin<sup>3†</sup>, Jun-Yi Zhang<sup>4</sup>, Yuanyuan Zhao<sup>3</sup>, Haitian Zhao<sup>2</sup>, Zhe Qu<sup>2</sup>, Yigui Zhong<sup>5</sup>, Kozo Okazaki<sup>5</sup>, Xiquan Zheng<sup>6</sup>, Yingying Peng<sup>6</sup>, Zurab Guguchia<sup>7</sup>, X. X. Wu<sup>8</sup>, Qianghua Wang<sup>9</sup>, X-H Fan<sup>1</sup>, Wei Song<sup>1</sup>, M-W Gao<sup>1</sup>, Hendrik Hohmann<sup>10</sup>, Matteo Dürnagel<sup>10,11</sup>, Ronny Thomale<sup>10</sup>, Jia-Xin Yin<sup>1,3†</sup>

### Affiliations:

<sup>1</sup>Department of Physics and Guangdong Basic Research Center of Excellence for Quantum Science, Southern University of Science and Technology, Shenzhen 518055, China

<sup>2</sup>Anhui Key Laboratory of Low-Energy Quantum Materials and Devices, High Magnetic Field Laboratory of Chinese Academy of Sciences, Hefei 230031, Anhui, China

<sup>3</sup>Quantum Science Center of Guangdong-Hong Kong-Macao Greater Bay Area, Shenzhen, China.

<sup>4</sup>William H. Miller III Department of Physics and Astronomy, Johns Hopkins University, Baltimore, Maryland 21218, USA

<sup>5</sup>Institute for Solid States Physics, The University of Tokyo, Kashiwa, Japan.

<sup>6</sup>International Center for Quantum Materials, School of Physics, Peking University, Beijing 100871, China

<sup>7</sup>Laboratory for Muon Spin Spectroscopy, Paul Scherrer Institute, CH-5232, Villigen PSI, Switzerland.

<sup>8</sup>CAS Key Laboratory of Theoretical Physics, Institute of Theoretical Physics, Chinese Academy of Sciences, Beijing 100190, China.

<sup>9</sup>National Laboratory of Solid State Microstructures & School of Physics, Nanjing University, Nanjing 210093, China.

<sup>10</sup>Institute for Theoretical Physics and Astrophysics, University of Würzburg, 97074 Würzburg, Germany.

<sup>11</sup>Institute for Theoretical Physics, ETH Zürich, 8093 Zürich, Switzerland.

\*These authors contributed equally to this work.

†Corresponding authors. E-mail: yinjax@sustech.edu.cn, qinhailang@quantumsc.cn

**The pair-density-wave (PDW) exhibits periodic amplitude and sign modulations of the superconducting order parameter. Such a pairing state has been proposed to be sensitive to nonmagnetic scattering. In this work, we observe the nonmagnetic PDW-breaking effect in a kagome superconductor, using scanning tunneling microscopy. We observe  $2\times 2$  PDW induced by the coupling between charge order and superconductivity. The global PDW is substantially suppressed upon doping the kagome lattice with dilute isovalent nonmagnetic impurities, whereas the charge order and uniform superconductivity remain robust. Spatial correlation analysis further confirms that PDW is distinctly suppressed near dopants. We attribute the PDW suppression to a nonmagnetic PDW breaking effect, arising from phase sign modulation of PDW in the kagome  $d$ -orbital hosting Bogoliubov Fermi states.**

Conventional superconductivity is robust against nonmagnetic scattering as dictated by the Anderson theorem, and the pair-breaking effect induced by nonmagnetic impurities often signals the presence of an unusual superconducting order. The PDW is a kind of unconventional superconducting order [1], where the Cooper pairs carry finite momentum. A distinguishing feature of the intrinsic pair density wave (primary or induced) is the spatial phase sign modulation of the superconducting order parameter [Fig. 1(a)]. Such a pairing state is then gapless, and has long been proposed to be highly sensitive to nonmagnetic impurity scattering [2-4]. It has recently been recognized that pair-breaking scattering interference is an alternative mechanism for pairing modulations [5]. However, such modulations do not feature phase sign reversal and can be promoted with

increasing impurity scattering. Therefore, the nonmagnetic impurity effect can serve as phase-sensitive evidence for PDW, which has been critically lacking in experiments.

Recent measurements have uncovered that  $AV_3Sb_5$  ( $A = K, Rb, Cs$ ) may host intrinsic PDW with phase sign modulations [6,7]. The ultra-low temperature tunneling spectroscopy [6-9], thermal transport [10], muon spin rotation [11] and nuclear quadrupole resonance [12] reveal gapless excitations; normal and Josephson scanning tunneling spectroscopy [6,7] reveal  $2\times 2$  pairing modulations as a result of the coupling between uniform superconductivity in the Sb  $p$ -orbital and  $2\times 2$  charge order in the V  $d$ -orbital; and ultra-low temperature angle-resolved photoemission spectroscopy [13] reveals strong anisotropic pairing gap in the V  $d$ -orbital and isotropic pairing gap in the Sb  $p$ -orbital; device-based chiral superconducting transport [14] and magnetic field tunability of the chirality of pairing modulations [6] further support time-reversal symmetry-breaking. These experimental progresses advance the theoretical understanding of the intertwined kagome orders [6,15-17], which have explained the gapless excitations as Bogoliubov Fermi states of the PDW order, and linked the anisotropic pairing with the modulated PDW gap. In this work, we further provide spectroscopic phase-sensitive evidence for the PDW. We select the kagome superconductor  $KV_3Sb_5$  as the clean platform [18], and we find that the nonmagnetic isovalent dopant Ta can be successfully doped into  $KV_3Sb_5$  single crystals up to 4%, grown with a self-flux method [19,20]. Through susceptibility and transport measurements in Fig. 1(b), we observe that the charge order is slightly suppressed while the superconductivity is substantially enhanced.

We then conduct dilution-refrigerator-based scanning tunneling microscopy experiments on these crystals at a lattice temperature of 30mK and electronic temperature estimated as 90mK. The underlying Ta dopant can be individually resolved in a high-bias-voltage image [21] of the Sb surface [Fig. 1(c)], which tightly bonds with the V kagome lattice. The concentration of the randomly distributed bright spots in the image matches the nominal Ta doping value of 4%. The zoomed-in image of each bright spot reveals that it is centered between two surface Sb atoms, aligning with the underlying V atomic position in the kagome lattice. The  $2\times 2$  charge order can be revealed by the low-bias (50mV, an energy close to the charge order gap) topographic image in Fig. 1(d). A comparison of the topographic data with pristine sample reveals that the  $2\times 2$  charge order is robust [Fig. 1(e) and Fig. S3], consistent with the robust charge order detected by susceptibility. Moreover, we find that the tunneling spectrum at the superconducting energy scale alters dramatically, with the pairing gap substantially increased in the doped crystal [Fig. 1(f)], consistent with the enhanced superconductivity detected by transport.

The pairing condensate of the crystal is further supported by our tunneling experiment using a superconducting Nb tip, revealing a much larger total pairing gap [Fig. 1(g)]. We detect a zero-bias peak in the differential conductance by reducing the tip-sample distance and the characteristic double kink features in the related current-voltage spectrum, both of which serve as key signatures of the Josephson tunneling signal and indicate the Cooper pair tunneling between two superconductors [6,8,22-24]. We have noticed the increasing conductance between the Josephson peak and coherence peaks, which has been repeatedly seen in the Josephson tunneling between kagome superconductors and a Nb tip [6,8]. It is likely related to the residual Fermi states in the kagome superconductor and remains an open question. We confirm that there is no noticeable change in the sample area after taking the spectra after reducing the tip-sample distance.

The scanned Josephson tunneling signal can detect the spatial modulation of the phenomenologically defined Cooper pair density [6,25] and provide evidence for PDW. Particularly, for superconductor with smaller energy gap, the pair density can be effectively detected [6,24] by  $N_J(r) \propto g_J(r, E = 0) \times R_N^2(r)$ , where  $g_J(r, E = 0)$  is the spatially resolved zero-bias peak in the differential conductance data at position  $r$  and  $R_N(r)$  is the spatially resolved Josephson junction normal state resistance at a bias where the current-voltage characteristics are linear.

The scanned pair density  $N_J(r)$  data on the Sb surface with atomic resolution is shown in Fig. 1(h). The corresponding Fourier transform data  $N_J(q)$  in right panel of Fig. 1(h) demonstrates the existence of  $2\times 2$  PDW in the material, which is expected from the intertwining between  $2\times 2$  charge order and superconductivity.

A straightforward interplay of the slightly weakened charge order  $\rho_Q$  and substantially enhanced uniform superconductivity  $\Delta_0$  predicts an enhanced PDW order  $\Delta_{\text{PDW}} \propto \rho_Q \Delta_0$  by Ginzburg-Landau theory, an intriguing phenomenon to explore. Unexpectedly, a comparison of this  $2\times 2$  pair density vector peak measured under similar conditions for pristine [6] and doped samples in Fig. 2(a) reveals that the global  $2\times 2$  pair density modulation is suppressed. To validate this striking observation of PDW suppression, we measure the modulations of the pairing gap with a normal tip. We measure the low-energy differential conductance  $g(r, E)$  along a line shown in Fig. 2(b). Through precise measurements of the superconducting coherence peaks, we detect tiny modulations in their energy positions. We extract the energy positions of the coherence peaks to obtain the modulation of the pairing gap  $\Delta(r)$  as shown in the right panel of Fig. 2(b), which is compared with the pristine sample [6]. It is evidence that the  $2a$  pairing gap modulation is also substantially suppressed by Ta dopants. To quantify this finding, we measure the gap modulations in the two-dimensional gap map, and the  $2\times 2$  modulation of the pairing gap is revealed by their Fourier transformation analysis in Fig. 3(c), demonstrating that the global  $2\times 2$  pairing gap modulation is substantially suppressed, which is rather consistent with the  $2\times 2$  pair density suppression. The pairing modulation at the Bragg vector is widely observed in experiments on other superconductors [6,8,23-29]. Its robustness against Ta dopants in absolute value suggests a trivial origin of the modulation at Bragg vector (without sign-reversals).

Thus, both the pair density modulation and pairing gap modulation reveal a strongly suppressed PDW, which contrasts with the simple estimation  $\Delta_{\text{PDW}} \propto \rho_Q \Delta_0$  by Ginzburg-Landau theory. In the pristine sample, quasi-particle interference imaging of the in-gap zero-energy states reveals segmented arcs, with high-temperature data linking them to parts of the reconstructed V  $d$ -orbital states within the charge order [6,7]. The residual Fermi arcs are explained by the partial suppression of these  $d$ -orbital states through an interorbital  $2\times 2$  PDW and thus serve as candidate Bogoliubov Fermi states [6,7,16] to elucidate the finite momentum pairing. We also measure this quasi-particle interference data in the doped sample and find that the residual arc-like signals are suppressed [Fig. 2(d)], aligning with the strong PDW suppression.

To gain microscopic insight, we investigate the spatial correlation between intertwined orders and atomic dopants. At the same atomic position, we obtain a topographic image at high bias voltage to reveal the locations of the Ta dopants [Fig. 3(a)], a topographic image at intermediate voltage to reveal the  $2\times 2$  charge order [Fig. 3(b)], and the low-energy superconducting gap map with ultra-high spatial energy resolution [Fig. 3(c)]. The Fourier transform of the gap map reveals the  $2\times 2$  PDW order [Fig. 3(c) inset]. Spanning such a large energy range is a nontrivial task. In many of our trials, the tip either crashes into the sample or deposits clusters onto it, especially when using the Nb tip, which always damages the crystal at a high bias voltage (thus we are not able to image Ta dopants with Nb tip). Proper preparation of a robust and atomically sharp tip is crucial to obtain a complete data set for three intertwined orders and dopant's position.

An inverse Fourier transform of the  $2\times 2$  vector peaks in the gap map extracts the  $2\times 2$  gap modulation [Fig. 3(d)], revealing spatial inhomogeneity of PDW. Larger local  $2\times 2$  gap modulations correspond to the larger local PDW order. We then extract the local amplitude of the  $2\times 2$  pairing gap modulation, which defines the local PDW strength, as shown in Fig. 3(e). Electronic inhomogeneity is often associated with unconventional ground states and correlated with dopant's position. Therefore, we mark the previously determined atomic dopant position on the PDW map in Fig. 3(e). By visual inspection, we observe that most of the dopant positions appear to correlate with regions of smaller PDW order. We similarly obtain the charge order map in Fig. 3(f) by

extracting the local amplitude of the  $2\times 2$  modulations from Fig. 3(b). Then, we perform a cross-correlation analysis between the charge order map [Fig. 3(f)], pairing gap map [Fig. 3(c)], PDW map [Fig. 3(e)], and dopant's position [extracted from Fig. 3(a)], respectively. Figure 3(g) shows that the PDW uniquely exhibits a moderate anticorrelation with the dopant's position. We also note that the existence of global PDW breaking can blur each local effect, which may explain why the anti-correlation coefficient is not super strong.

The positive correlation between charge order and dopant's position in Fig. 3(g) could be attributed to the weaker impurity-pinning effect [30]. This observation also suggests that the slight global charge order suppression likely originates from a nonlocal mechanism, such as the phonon. In Fig. 3(h), we further show that the local superconducting gap is also robust at the Ta dopant site. It supports the nonmagnetic nature of the Ta dopants (see also Fig. S6). The contrast correlation behavior demonstrates that the local PDW suppression near Ta dopants does not result from the trivial cause of local suppression of charge order or superconductivity. The unique local PDW suppression together with strong global PDW suppression highlights a nonmagnetic PDW breaking effect.

We discuss the mechanism of the nonmagnetic PDW breaking effect. The kagome intertwined orders features unique orbital-selectivity [6,7]: the  $2\times 2$  charge order mainly occurs in the kagome V  $d$ -orbital; uniform superconductivity mainly occurs in the Sb  $p$ -orbital [6,7,13], but not the V  $d$ -orbital (otherwise the residual Fermi arcs would be gapped out), likely owing to the time-reversal symmetry-breaking of the kagome charge order [31]; the coupling of the two orders produces a  $2\times 2$  PDW with corresponding Bogoliubov Fermi arcs in the  $d$ -orbital [6,7,16,32]. Such PDW pairing featuring Bogoliubov Fermi states will not only spatially modulate the amplitude of the order parameter, but also the phase signs [16] [as illustrated in Fig. 3(i)]. It has long been proposed that such kind of PDW order with phase sign reversals is highly sensitive to nonmagnetic impurity scattering [2-4]. Nonmagnetic impurities cause scattering between states with different momenta and phases, thereby tending to destroy the corresponding spatial modulations [2-4]. This physics is further confirmed by our study of the nonmagnetic PDW-breaking effect using the Abrikosov-Gor'kov approach (Fig. S7). Thus, we attribute the striking PDW suppression to the nonmagnetic PDW-breaking effect, originating from the phase modulation of the PDW order in the kagome  $d$ -orbital. The nonmagnetic PDW-breaking phenomenon is a fundamental quantum effect of PDW, and we look forward to using this effect to test the proposed PDW in other systems.

## Figures

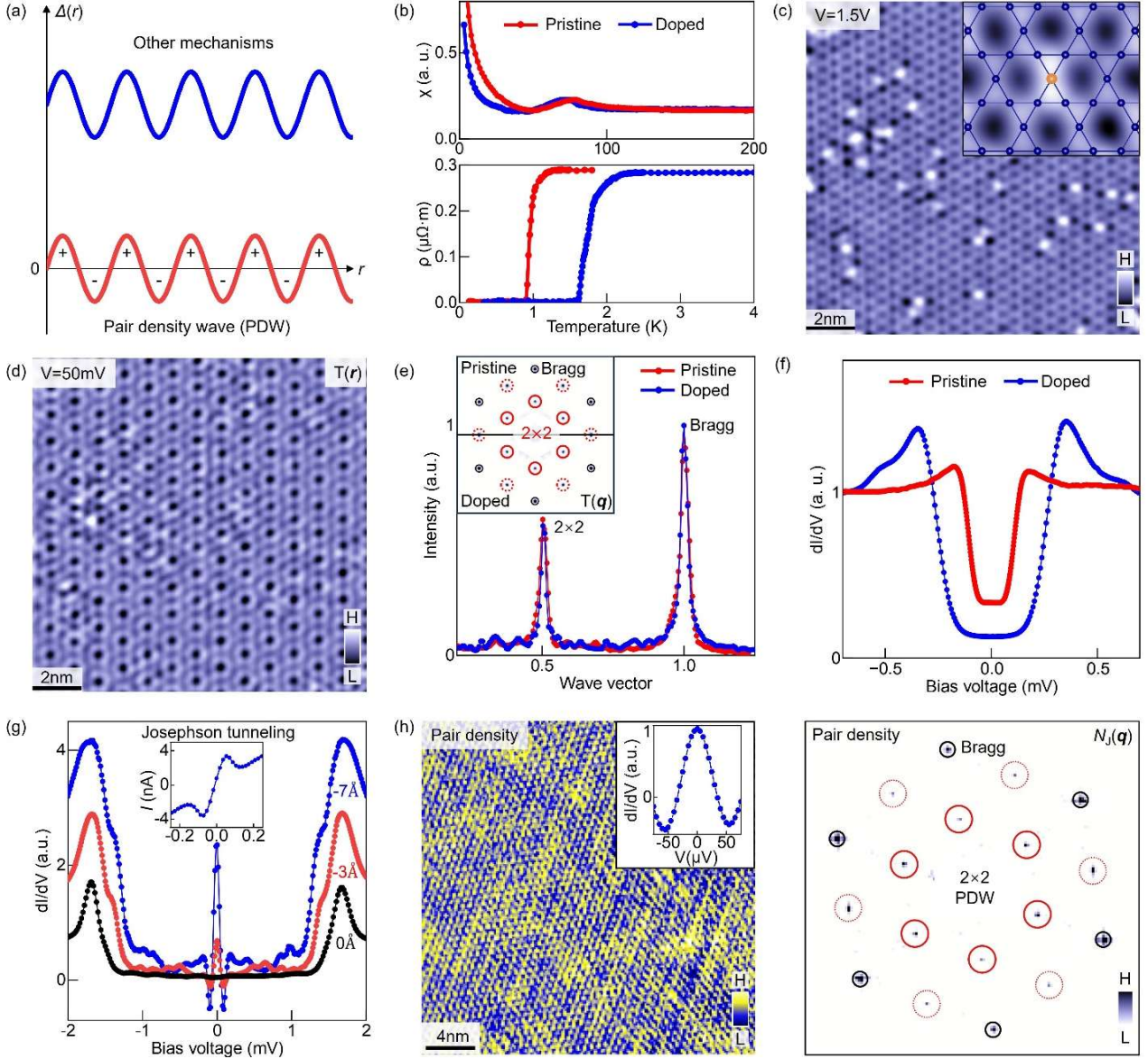


FIG. 1. (a) Comparison between PDW and pairing modulations produced by other mechanisms. The PDW features a phase sign modulation in real space. (b) The upper panel compares the susceptibility data on charge order transition. The lower panel compares the resistivity data on superconducting transition. (c) Topographic image of the Sb surface under a high bias voltage, showing individual Ta dopants as bright spots. The inset shows the zoomed-in image of a bright spot and the indication of the atomic details, showing its consistency with a Ta dopant in the underlying kagome lattice. (d) Topographic image of the Sb surface under a low bias voltage, showing the  $2\times 2$  charge order. (e) The inset compares the Fourier transform of topography for a larger area, revealing  $2\times 2$  charge order, marked by red circles. Black circles indicate Bragg peaks, and the red dashed circles highlight higher-order peaks. The main panel compares the corresponding vector peaks, where both data are rotationally symmetrized from inset. (f) Comparison of the superconducting gap for pristine and doped samples. (g) Differential conductance taken with reducing the tip-sample distance from  $0\text{\AA}$  to  $-7\text{\AA}$  in reference to normal condition using a superconducting Nb tip, showing Josephson signal at zero bias. The inset shows a typical  $I-V$  curve. (h) Pair density map (left, inset shows the Josephson zero-bias peak signal) and its Fourier transform (right), exhibiting  $2\times 2$  PDW.

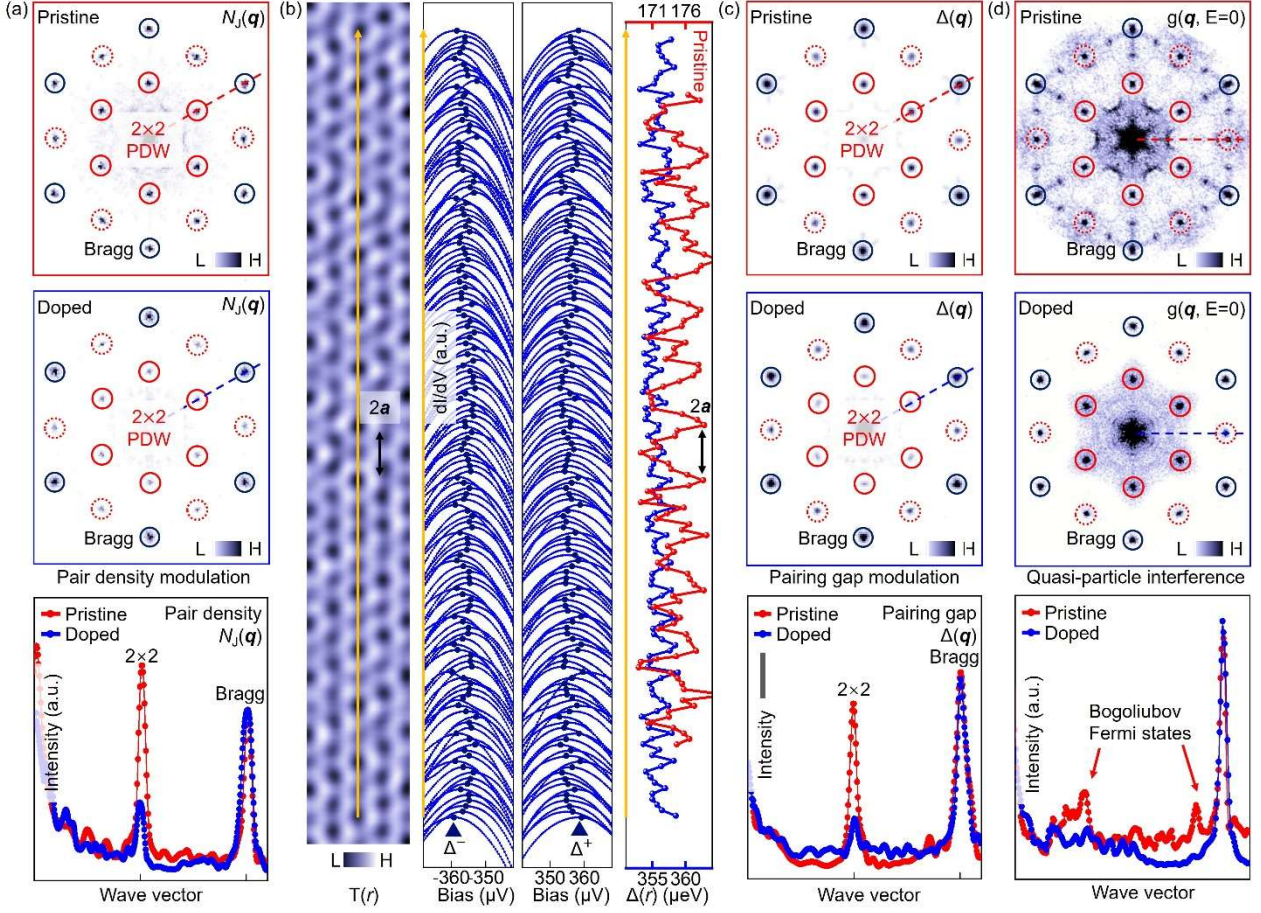


FIG. 2. (a) Comparison of the pair density modulation data for the pristine (upper panel) and doped (middle panel) samples in the  $q$ -space. Both data are rotationally symmetrized. Their intensities along the dashed lines are compared in the lower panel, showing strong reduction of the  $2 \times 2$  pair density modulation. (b) High-resolution spectra (middle) near the superconducting gap edge, along the line drawn in the topographic image (left) obtained with a normal tip.  $\Delta^\pm(r)$  is determined from the energy position of the peak, as indicated by the dark blue dots. The right panel shows the extracted pairing gap modulations  $\Delta(r) = [\Delta^+(r) - \Delta^-(r)]/2$ , which is further compared with the gap modulations of the pristine sample (energy scale noted in upper axis with same energy segregation ratio). (c) Comparison of the pairing gap modulation data for the pristine (upper panel) and doped (middle panel) samples in the  $q$ -space. Both data are rotationally symmetrized. Their intensities along the dashed lines are compared in the lower panel, showing strong reduction of the  $2 \times 2$  pairing gap modulation. The vertical bar denotes a value whose inverse Fourier transform corresponds to a modulation amplitude of  $2\mu\text{eV}$  (from peak to bottom). (d) Comparison of the quasi-particle interference data taken at zero energy for the pristine (upper panel) and doped (middle panel) samples in the  $q$ -space. Both data are rotationally symmetrized. Their intensities along the dashed lines are compared in the lower panel, showing the suppression of candidate Bogoliubov Fermi arc states.

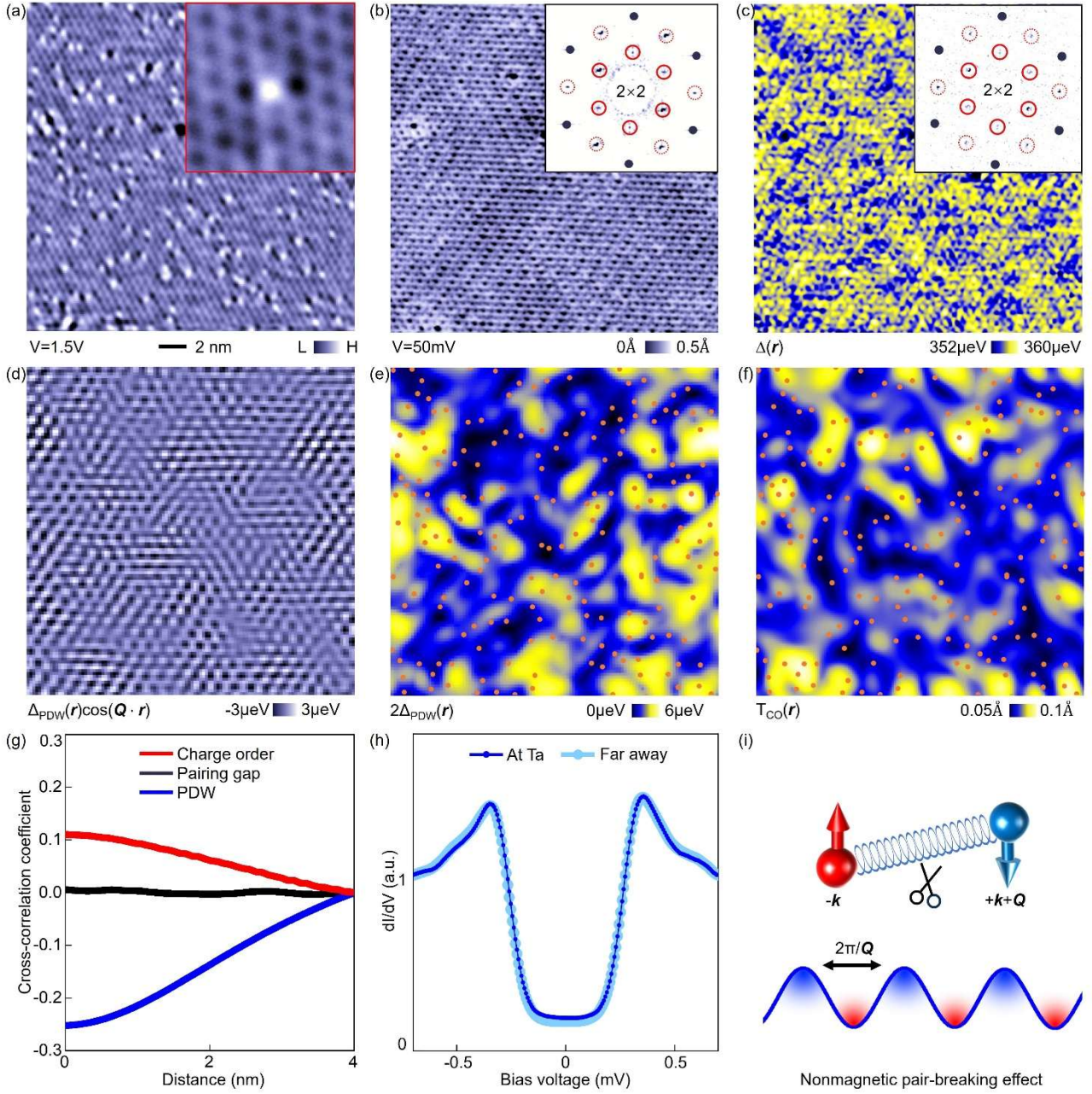


FIG. 3. (a) High bias topography with a zoomed-in Ta dopant shown in inset. (b) Low bias topography with its Fourier transform in inset showing the  $2 \times 2$  charge order. (c) Pairing gap map at the same position. The inset displays its Fourier transform, showing the  $2 \times 2$  PDW order. (d) Inverse Fourier transform of the  $2 \times 2$  vector peaks from the gap map, showing  $2 \times 2$  gap modulations. (e) PDW map obtained by extracting the local amplitude of the  $2 \times 2$  gap modulations. The dots indicate dopants. (f) Charge order map obtained by extracting the local amplitude of the  $2 \times 2$  charge modulations. The dots indicate dopants. (g) Cross-correlation coefficient between the charge order, pairing gap, and PDW and dopant's position, respectively. The PDW order uniquely shows a moderate anti-correlation with the dopant's position. (h) Comparison of the superconducting gap at dopant and distant positions. (i) Illustration of the nonmagnetic PDW-breaking effect, arising from the phase-sign reversal of the order parameter.

## References

- [1] D. F. Agterberg *et al.*, *Annu. Rev. Condens. Matter Phys.* **11**, 231 (2020).
- [2] L. G. Aslamazov, *Sov. Phys. JETP* **28**, 773 (1969).
- [3] S. Takada, *Prog. Theor. Phys.* **43**, 27 (1970).
- [4] Q. Cui and K. Yang, *Phys. Rev. B* **78**, 054501 (2008).
- [5] Z.-Q. Gao, Y.-P. Lin, and D.-H. Lee, *Phys. Rev. B* **110**, 224509 (2024).
- [6] H. B. Deng *et al.*, *Nature* **632**, 775 (2024).
- [7] X. Y. Yan *et al.*, *Chin. Phys. Lett.* **41**, 097401 (2024).
- [8] H. Chen *et al.*, *Nature* **599**, 222 (2021).
- [9] H.-S. Xu *et al.*, *Phys. Rev. Lett.* **127**, 187004 (2021).
- [10] C. C. Zhao *et al.*, *Chin. Phys. Lett.* **41**, 127303 (2024).
- [11] Z. Guguchia *et al.*, *Nat. Commun.* **14**, 153 (2023).
- [12] X. Y. Feng *et al.*, *Nat. Commun.* **16**, 3643 (2025).
- [13] A. Mine *et al.*, Preprint at arXiv:2404.18472 (2024).
- [14] T. Le *et al.*, *Nature* **630**, 64 (2024).
- [15] R. Tazai, Y. Yamakawa, S. Onari, and H. Kontani, *Sci. Adv.* **8**, eabl4108 (2022).
- [16] M. Yao, Y. Wang, D. Wang, J.-X. Yin, and Q.-H. Wang, *Phys. Rev. B* **111**, 094505 (2025).
- [17] S. C. Holbæk and M. H. Fischer, *Phys. Rev. Res.* **7**, 023129 (2025).
- [18] B. R. Ortiz, P. M. Sarte, E. M. Kenney, M. J. Graf, S. M. L. Teicher, R. Seshadri, and S. D. Wilson, *Phys. Rev. Materials* **5**, 034801 (2021).
- [19] Y. Zhong *et al.*, *Nature* **617**, 488 (2023).
- [20] H. B. Deng *et al.*, *Nat. Mater.* **23**, 1639 (2024).
- [21] P. Wu *et al.*, *Nat. Phys.* **19**, 1143 (2023).
- [22] O. Naaman, W. Teizer, and R. C. Dynes, *Phys. Rev. Lett.* **87**, 097004 (2001).
- [23] M. H. Hamidian *et al.*, *Nature* **532**, 343 (2016).
- [24] X. Liu, Y. X. Chong, R. Sharma, and J. C. S. Davis, *Science* **372**, 1447 (2021).
- [25] L. Cao, Y. Xue, Y. Wang, F.-C. Zhang, J. Kang, H.-J. Gao, J. Mao, and Y. Jiang, *Nat. Commun.* **15**, 7234 (2024).
- [26] Z. Du, H. Li, S. H. Joo, E. P. Donoway, J. Lee, J. C. S. Davis, G. Gu, P. D. Johnson, and K. Fujita, *Nature* **580**, 65 (2020).
- [27] H. Zhao *et al.*, *Nature* **618**, 940 (2023).
- [28] Y. Liu, T. Wei, G. He, Y. Zhang, Z. Wang, and J. Wang, *Nature* **618**, 934 (2023).
- [29] Q. Gu *et al.*, *Nature* **618**, 921 (2023).
- [30] P. A. Lee, T. M. Rice, and P. W. Anderson, *Solid State Commun.* **14**, 703 (1974).
- [31] C. Mielke III *et al.*, *Nature* **602**, 245 (2022).
- [32] Y.-F. Jiang, H. Yao, and F. Yang, *Phys. Rev. Lett.* **127**, 187003 (2021).

**Acknowledgments:** We thank Mark H. Fischer, Sofie Castro-Holbæk, Manfred Sigrist, Hong Yao, Fuchun Zhang, Congjun Wu, Hu Miao, S. S. Islam, Yang Gao, Sen Zhou, Andreas Kreisler, and Brian Møller Andersen for discussions. J.Y.Z. acknowledge the encouragement and support from Yi Li. We acknowledge the support from the National Key R&D Program of China (grant numbers 2023YFA1407300).

## Supplemental Material for “Phase-sensitive evidence for pair density wave in a kagome superconductor”

### 1. Single crystal growth

Single crystals of Ta-doped  $\text{KV}_3\text{Sb}_5$  were grown using the self-flux method from the constituent elements. High-purity K, V, Ta, and Sb were mixed in an alumina crucible in a molar ratio of 5:2.7:0.3:13 and sealed in an evacuated quartz ampoule. The ampoule was heated to 1273K, soaked for 20h, then cooled down to 923K at 2K/h. Residual flux was removed by centrifugation. The chemical composition of the as-grown single crystals was determined to be  $\text{K}(\text{V}_{0.96}\text{Ta}_{0.04})_3\text{Sb}_5$  via energy-dispersive X-ray spectroscopy, and checked with the topographic data in scanning tunneling microscopy. Single crystal X-ray diffraction measurements were conducted using the custom-designed X-ray instrument at 20K. The lattice parameters for  $\text{KV}_3\text{Sb}_5$  are determined to be  $a = b = 5.464\text{\AA}$ ,  $c = 8.909\text{\AA}$ , while for 4% Ta-doped  $\text{KV}_3\text{Sb}_5$ , the lattice parameters are  $a = b = 5.464\text{\AA}$ ,  $c = 8.899\text{\AA}$ .

### 2. Normal and Josephson scanning tunneling microscopy

Over 40 crystals were cleaved and imaged in this project, where most cleaved crystals are used to explore the suitable conditions for tunneling at various voltages for different purpose. Crystals with dimensions up to  $2\text{mm}\times 2\text{mm}\times 0.5\text{mm}$  are cleaved mechanically *in-situ* at 77K under ultra-high vacuum conditions and immediately inserted into the microscope head, which is pre-cooled to the  $\text{He}^4$  base temperature of 4.2K. The microscope head is then further cooled to 30mK using a dilution refrigerator. The cooling procedure takes about 12h. Tunneling conductance spectra are obtained with Ir/Pt tips (or a superconducting tip, as described below) using standard lock-in amplifier techniques. Each crystal is extensively scanned to identify large, clean Sb surfaces, which typically takes a week to find. Topographic images are typically obtained with a tunneling junction set to  $V = 50\text{mV}$ ,  $I = 0.5\text{nA}$ . To image the individual Ta dopants, the topographic images are taken with a tunneling junction set to  $V = 1.5\text{V}$ ,  $I = 0.5\text{nA}$ . Conductance and gap maps are acquired by taking a spectrum at each location (with the feedback loop off) with a tunneling junction set of:  $V = 1\text{mV}$ ,  $I = 1\text{nA}$ , and modulation voltage  $V_m = 3\sim 20\mu\text{V}$ . These tunneling conditions further require a clean sample area and stable, atomic-resolution tunneling tips. One method of preparing a stable tip is to anneal them on an Au crystal under similar tunneling conditions, ensuring the tip is robust.

We discuss the spatial energy resolution of scanning tunneling microscopy. To estimate the electronic temperature of our system, we measure the superconducting gap of a related full-gap kagome superconductor (14%-Ta doped  $\text{CsV}_3\text{Sb}_5$ ) with similar setup. By fitting the superconducting gap to the BCS gap function (Fig. S1), we estimate the electronic temperature to be approximately 90mK. The commonly discussed energy resolution,  $\Delta E$ , can be understood as follows: if an electronic state exhibits  $\delta$  function, then it will behave as a Gaussian-like function in the tunneling data, with a full width at half maximum of  $dE$  [Fig. S2(a)]. In our case,  $dE = 90\text{mK}\cdot 3.5k_B$ , where  $k_B$  is the Boltzmann constant. At a fixed position, if two such states have an energy separation smaller than  $dE$ , they will merge into a single peak in the tunneling data, making it impossible to distinguish the two states directly [Fig. S2(b)]. However, if these states are located at different locations, their spectral peak energy difference, although broadened, may still be distinguished by scanning tunneling spectroscopy [Fig. S2(c)]. In this case, both the spatial resolution of the tunneling tip and the signal-to-noise ratio of the tunneling spectrum are as crucial as the electronic energy resolution  $dE$ , which can be improved by maintaining a stable tunneling condition and elongating the measuring time. In the present case, we find that scanning tunneling microscopy can resolve the spatial modulations of superconducting coherence peaks at  $\mu\text{eV}$

level. For similar reasons, previous studies [6,8,25,29] achieve 1~10 $\mu$ eV level spatial energy resolution in studying PDW even at a lattice temperature of 300~400mK. In principle, the higher the electronic temperature, the flatter the measured peak, and a higher signal-to-noise ratio is required. And if the sample's coherence peak is too broad, then a superconducting tip can help to enhance the sharpness of the measured coherence peak, enhancing the signal-to-noise ratio for determining the peak energy (or enhance the effective "energy resolution"). In our case, the sample's coherence peak is narrower than that of Nb, and with a Nb tip, the measured coherence peak is actually broader, which does not contribute to an effective higher energy resolution in determining the PDW gap modulations. This is also the reason we measure the pairing gap map with normal tip.

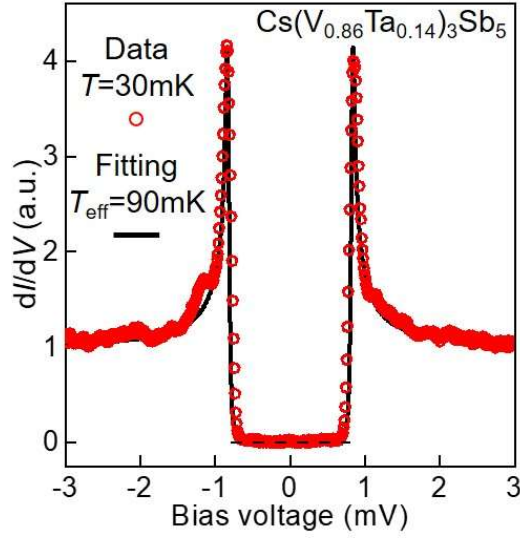


FIG. S1. Fitting the superconducting gap of  $\text{Cs}(\text{V}_{0.86}\text{Ta}_{0.14})_3\text{Sb}_5$  single crystal with the BCS gap function ( $V = 1$  mV,  $I = 1$  nA,  $V_m = 20$   $\mu$ V). The fit estimates the electronic temperature of our system to be 90mK.

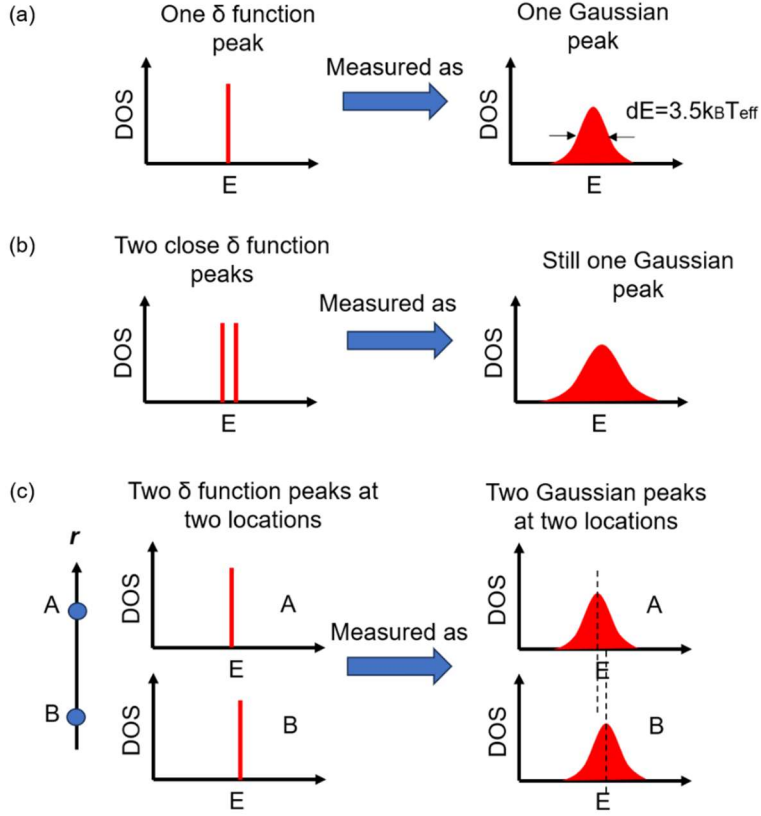


FIG. S2. (a) A  $\delta$  function state is measured as a Gaussian-like peak in the tunneling spectrum due to the convolution effect with a derivative of the Fermi-Dirac distribution function. The Gaussian-like peak has a finite width of  $dE = 3.5k_B T_{\text{eff}}$ , where  $k_B$  is the Boltzmann constant and  $T_{\text{eff}}$  is the effective electronic temperature of the system. (b) If two close  $\delta$  function states exist, they will be measured as a single Gaussian-like peak when their energy separation is smaller than  $dE$ . In this case, tunneling spectroscopy cannot distinguish the two states due to finite electronic temperatures. (c) If two close  $\delta$  function states are located differently at real space, they can be measured as two Gaussian-like peaks (one at each location). Their peak energy difference may be smaller than  $dE$ , depending on the measurement accuracy. To resolve both peaks, the following conditions are required: i) high spatial resolution to prevent peak merging, and ii) high signal-to-noise ratio to accurately determine the peak energy positions. For similar reasons, previous studies [6,8,25,29] can achieve  $\mu\text{eV}$  level spatial energy resolution in studying PDW even at a lattice temperature of 300~400mK.

Superconducting polycrystalline Nb tips were used for the Josephson scanning tunneling microscopy experiment. In order to prepare a superconducting Nb tip, we use electrochemical etching of Nb wires, followed by e-beam heating. More specifically, we use a NaOH solution with a concentration of  $\sim 52$  wt%, and etch the tip with an AC voltage of around 30~50V between the Nb wire (with a diameter of 0.3 mm) and carbon electrode for about 20 minutes, while the solution is maintained at about 90°C. After the etching, the tip is typically rinsed in de-ionized water before loading into the ultra-high vacuum chamber. The tip is then heated to an estimated temperature of 1500°C for about 10 seconds for ten times with electron-beam heating for further cleaning. To check the tip superconducting gap size and stability, we typically first test on a polycrystalline Pb sample by topographic imaging and taking  $dI/dV$  spectrums.

The pairing gap of the Nb tip is estimated to be 1.33meV based on the total gap size of the Josephson junction. Due to the complex surface environment (Sb surface mixed with K surfaces, adatoms, and other disordered surfaces), it is extremely challenging to maintain the superconductivity (pairing gap) of the tip with atomic resolution. We find that when a large bias voltage of 1.5V is applied to resolve the Ta dopant, the tip often crushes into the sample and loses its superconductivity properties. Therefore, topographic images are usually taken with the tunneling junction set to  $V = 50\text{mV}$   $I = 0.5\text{nA}$ . Josephson conductance spectra and maps are obtained by measuring the spectrum at each location (with the feedback loop off) using a tunneling junction setup of:  $V = 3\text{mV}$ ,  $I = 8\text{nA}$ , and modulation voltage  $V_m = 30\mu\text{V}$ . The zero-bias peak is readily observed at this junction setup and is further enhanced by increasing the tunneling current, as shown in Fig. 1. The Josephson coupling energy,  $E_J$ , is estimated to be  $20\text{mK} \cdot k_B$  (where  $k_B$  is the Boltzmann constant), which is smaller than the electronic temperature of the system 90mK, placing the Josephson junction close to the phase diffusive limit. In principle, the phenomenologically defined local pair density  $N_J(\mathbf{r})$  is expected to be proportional to the Josephson critical current  $I_J(\mathbf{r})$  times the normal state resistance  $R_N(\mathbf{r})$ :  $N_J(\mathbf{r}) \propto I_J^2(\mathbf{r})R_N^2(\mathbf{r})$ . However, for small gap superconductors where the Josephson coupling energy  $E_J$  is typically smaller than the electronic temperature, accurately measuring  $I_J$  is challenging. In such cases, the tunneling current takes the form:  $I = 0.5I_J^2 ZV / (V^2 + V_C^2)$ , where  $Z$  is the high-frequency impedance and  $V_C$  is the characteristic voltage at which the maximum phase-diffusive electron-pair tunneling current occurs. Then the differential conductance at zero energy is given by  $g_J(0) = dI/dV = 0.5I_J^2 V_C^{-2} \propto I_J^2$ . Thus,  $g_J(\mathbf{r}, E = 0)R_N^2(\mathbf{r})$  provides a practical method for measuring the pair density  $N_J(\mathbf{r})$  in small gap superconductors. Therefore, we measure both zero-bias conductance peak  $g_J(\mathbf{r}, E = 0)$  and normal-state junction resistance  $R_N(\mathbf{r})$  at each location  $\mathbf{r}$ . The normal-state resistance  $R_N(\mathbf{r})$  is determined as  $V/I(r, V)$ , where  $V$  is the sample bias at which the current-voltage characteristics are linear (typically at 3mV) and  $I(r, V)$  is the tunneling current at bias  $V$ .

### 3.Extended Data for charge order and PDW comparison with pristine sample

Fig. S3 shows the related topography for charge order, pair density maps, pairing gap maps and zero-energy quasi-particle interference maps for both pristine and doped crystals, as the extended data for Figs. 1 and 2 in the main text.

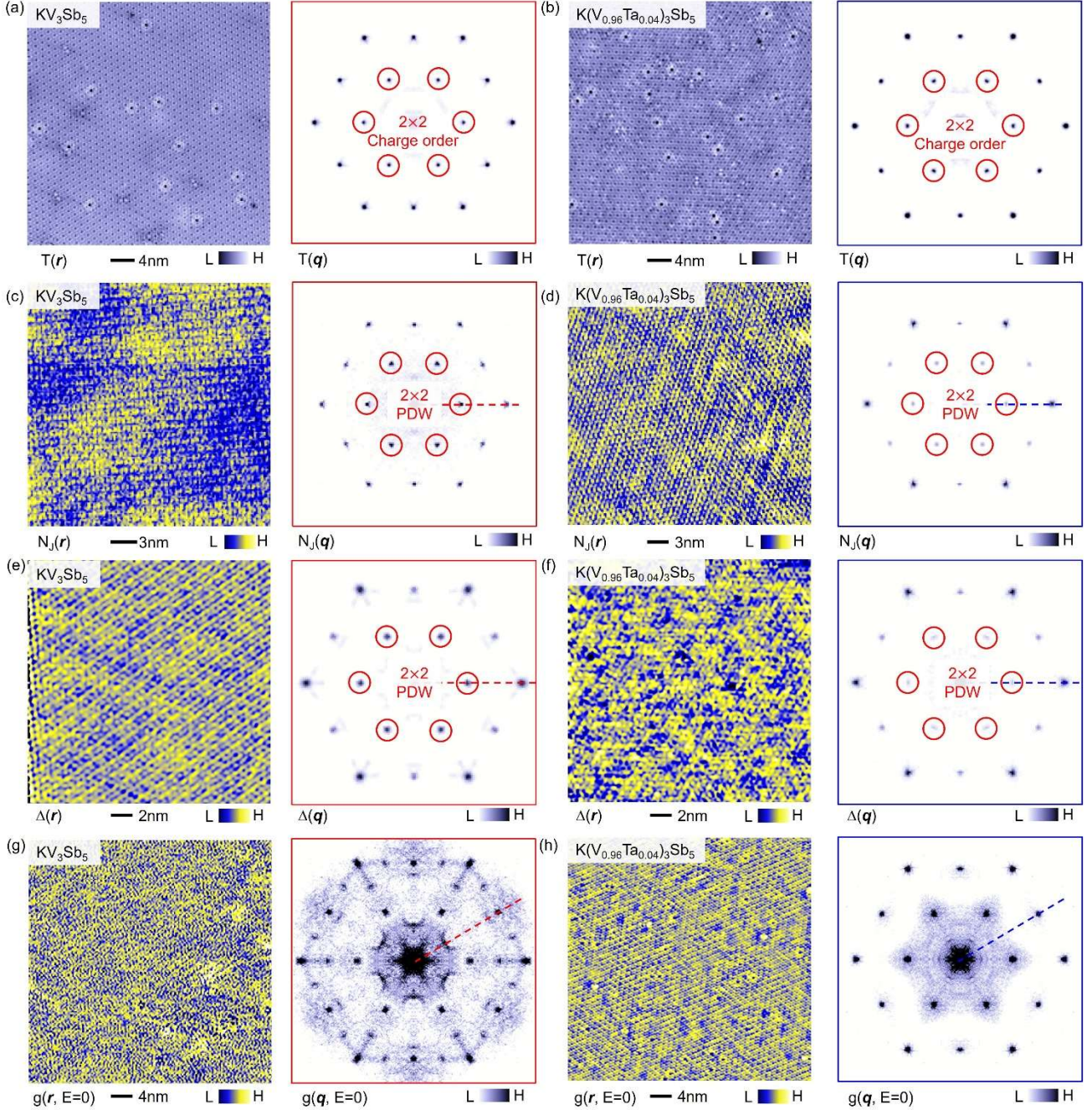


FIG. S3. (a), (b) The left data shows topography for measuring charge order for pristine and doped crystals, respectively ( $V = 50\text{mV}$ ,  $I = 0.5\text{nA}$ ). The right panel plots the related Fourier transform with six-fold symmetrization, showing  $2\times 2$  charge order. (c), (d) The left data shows pair density map measured with a Nb tip for pristine and doped crystals, respectively ( $V = 3\text{mV}$ ,  $I = 8\text{nA}$ ,  $V_m = 30\mu\text{V}$ ). The right panel plots the related Fourier transform with six-fold symmetrization. (e), (f) The left data shows the gap map measured with a normal tip for pristine and doped crystals, respectively ( $V = 1\text{mV}$ ,  $I = 1\text{nA}$ ,  $V_m = 3\mu\text{V}$ ). The right panel plots the related Fourier transform with six-fold symmetrization. (g), (h) The left data shows the zero-energy map measured with a normal tip for pristine and doped crystals, respectively ( $V = 1\text{mV}$ ,  $I = 1\text{nA}$ ,  $V_m = 50\mu\text{V}$ ). The right panel plots the related Fourier transform with six-fold symmetrization, showing the candidate Bogoliubov Fermi arc signals.

#### 4. Cross-correlation analysis and extended discussions

The pairing gap modulation in the real-space image consists of a series of modulation wavevectors:  $\Delta(\mathbf{r}) = \sum_{\mathbf{Q}} \Delta_{\mathbf{Q}}(\mathbf{r}) e^{-i\mathbf{Q}\cdot\mathbf{r}}$ , where  $\Delta_{\mathbf{Q}}(\mathbf{r})$  is the complex amplitude at wavevector  $\mathbf{Q}$  and position  $\mathbf{r}$ ;  $e$  is the Euler's number and  $i$  is the imaginary unit. The Fourier transform of this real-space image can be given by:  $\Delta(\mathbf{q}) = F[\Delta(\mathbf{r})] = \sum_{\mathbf{Q}} \int d\mathbf{q}' \Delta_{\mathbf{Q}}(\mathbf{q}') \delta(\mathbf{Q} - \mathbf{q} + \mathbf{q}') = \sum_{\mathbf{Q}} \Delta_{\mathbf{Q}}(\mathbf{q} - \mathbf{Q})$ , where  $\Delta_{\mathbf{Q}}(\mathbf{q} - \mathbf{Q})$  is the Fourier transform of the complex amplitude centered at  $\mathbf{Q}$ .  $\Delta_{\mathbf{Q}}(\mathbf{q})$  can be extracted by shifting it back to the center associated with wavevector  $\mathbf{Q}$ . The inverse Fourier transform of  $\Delta(\mathbf{q})$  can be written as:  $\Delta_{\mathbf{Q}}(\mathbf{r}) = F^{-1}[\Delta_{\mathbf{Q}}(\mathbf{q})] =$

$$F^{-1} \left[ F[\Delta(\mathbf{r}) e^{i\mathbf{Q}\cdot\mathbf{r}}] \cdot \frac{1}{\sqrt{2\pi}\sigma_q} e^{-\frac{q^2}{2\sigma_q^2}} \right],$$

where  $\sigma_q$  is the cutoff length, which is the inverse of the averaging length

scale in real space, but larger than the filter length at  $\mathbf{Q}$ . We collected the gap map  $\Delta_{\text{SC}}(\mathbf{r})$  as the real-space image  $\Delta(\mathbf{r})$ . We obtained the  $\Delta_{\text{SC}}(\mathbf{q})$  in  $q$ -space by applying a Fourier transform to the  $\Delta_{\text{SC}}(\mathbf{r})$ , where the  $\mathbf{Q}_i (i = 1, 2, 3)$  wavevectors at  $2 \times 2$  peaks reveal the PDW order. Using the two-dimensional lock-in method [26,28], we extract the local PDW order in real space associated with tentative modulation wavevector

$$\mathbf{Q}_i (i = 1, 2, 3): \quad \Delta_{\text{PDW}}(\mathbf{r}) = \sum_i \Delta_{\text{PDW}}^{\mathbf{Q}_i}(\mathbf{r}) = \sum_i F^{-1}[\Delta_{\text{SC}}^{\mathbf{Q}_i}(\mathbf{q})] = \sum_i F^{-1} \left[ F[\Delta_{\text{SC}}(\mathbf{r}) e^{i\mathbf{Q}_i\cdot\mathbf{r}}] \cdot \frac{1}{\sqrt{2\pi}\sigma_q} e^{-\frac{q^2}{2\sigma_q^2}} \right]. \quad A$$

similar method is used to extract the local charge order map in Fig. 3. Fig. S4 shows the inverse Fourier transform and charge order map data extracted from Fig. 3(b).

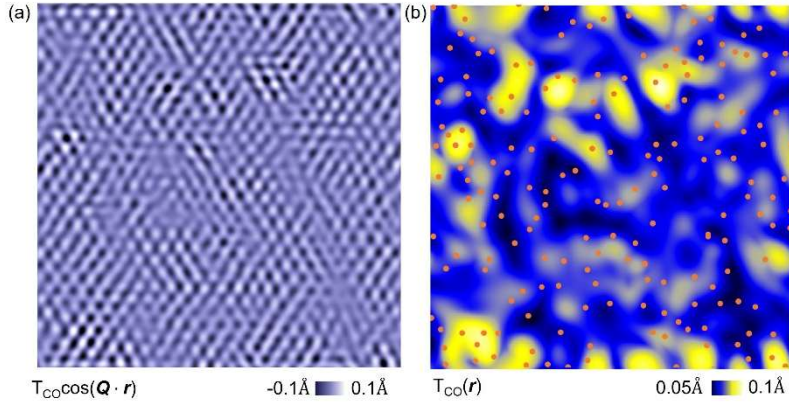


FIG. S4. (a) Inverse Fourier transform of the  $2 \times 2$  vector peaks from the topographic data in Fig. 3(b). (b) Charge order map obtained at the same atomic position, extracted from the local amplitude of the  $2 \times 2$  modulations. The red dots mark the atomic Ta dopants identified from Fig. 3(a).

To correlate the local PDW (or charge order) amplitude  $A(\mathbf{r})$  with the dopant position  $D(\mathbf{r})$ , we compute the cross-correlation  $C(\mathbf{r})$  using the standard formula:

$$C(\mathbf{r}) = \frac{\int [A(\mathbf{R}) - \langle A \rangle] \times [D(\mathbf{R} + \mathbf{r}) - \langle D \rangle] d^2 R}{\sqrt{\int [A(\mathbf{R}) - \langle A \rangle]^2 d^2 R \times \int [D(\mathbf{R}) - \langle D \rangle]^2 d^2 R}} \quad (1)$$

where  $\langle A \rangle$  and  $\langle D \rangle$  denote the spatial averages of the intensity map and dopant map, respectively. The resulting two-dimensional cross-correlation map  $C(\mathbf{R})$  quantifies how the local amplitude is modulated as a function of the distance from dopant sites. To further characterize the distance dependence, the correlation map was azimuthally averaged to yield a one-dimensional profile as a function of the distance  $r = |\mathbf{r}|$  from the dopant.

We also note that the cross-correlation analysis in Fig. 3(g) suggests that the PDW is suppressed by dopants within a characteristic length scale of 2nm, much larger than the superconducting coherence lengths in kagome superconductors ( $\sim 20\text{nm}$  or larger [6,9,20,33]). The deep physical meaning of this length is still less understood. Noting that we are in a region that there should be rich interference between individual local dopant PDW breaking effect, as the global PDW is readily suppressed substantially. In addition, the nonmagnetic PDW breaking effect resembles the nonmagnetic pair-breaking effect for a superconductor with sign reversals as in our analysis using Abrikosov-Gor'kov approach (see later text), which further resembles the magnetic pair-breaking effect in an *s*-wave superconductor. It could be a good reference to check in what length scale a magnetic impurity could affect the local superconducting density of states: the magnetic impurity introduces a bound state (together with suppression of coherence peaks) which decays in  $1/r^2 \exp(-r/\xi)$  in a three-dimensional superconductor, where  $\xi$  is the coherence length. Therefore, the spirit is that, unlike the vortex matter, the local impurity's impact could be much shorter than the coherence length due to the additional decay factor  $1/r^2$ , which could be a useful reference in the future complete understanding of the observed PDW suppression length scale. And we propose that the magnetic pair-breaking effect in this kagome superconductor by magnetic dopants can occur at a similar length scale, which can be tested in future.

### 5. First-principles calculations.

First-principles density-functional-theory (DFT) calculations are performed using the Vienna ab initio simulation package (VASP) which adopts the projector-augmented wave method [34]. The energy cutoff is set at 400eV and exchange-correlation functional of the Perdew-Burke-Ernzerhof (PBE) type [35] is used for the electronic structure calculations. The doping effects of Ta are treated in virtual-crystal approximation [36] as implemented in VASP. Phonopy code [37] together with finite-difference method are used for the calculations of the phonon spectrums, a  $3 \times 3 \times 2$  supercell and a  $5 \times 5 \times 3$  k-mesh is adopted.

Using the virtual-crystal approximation, we are able to grasp the main features of the electronic structures of  $\text{KV}_3\text{Sb}_5$  as a function of Ta doping. From Fig. S5(a), we can see that at 4% doping of Ta, the overall low-energy electronic structures show no obvious changes. Under such Fermi surfaces, the charge order transition temperature can be roughly captured by the smearing temperature adopted during DFT calculations of the phonon spectrum. With increasing smearing  $\sigma$ , the soft phonon modes around the M and L points gradually becoming harder, as shown in Fig. S5(b). The charge order transition temperature  $T^*$  sets the onset where the soft mode disappears. By including the anharmonic corrections [38], we are able to track  $T^* \sim 120\text{K}$  for the pristine sample, which is of the same order as that detected in experiments. We then calculate  $T^*$  as a function of the doping, we find that doping 4% Ta to  $\text{KV}_3\text{Sb}_5$  will reduce  $T^*$  by 7%, which aligns with the experimentally observed slight reduction of charge order.

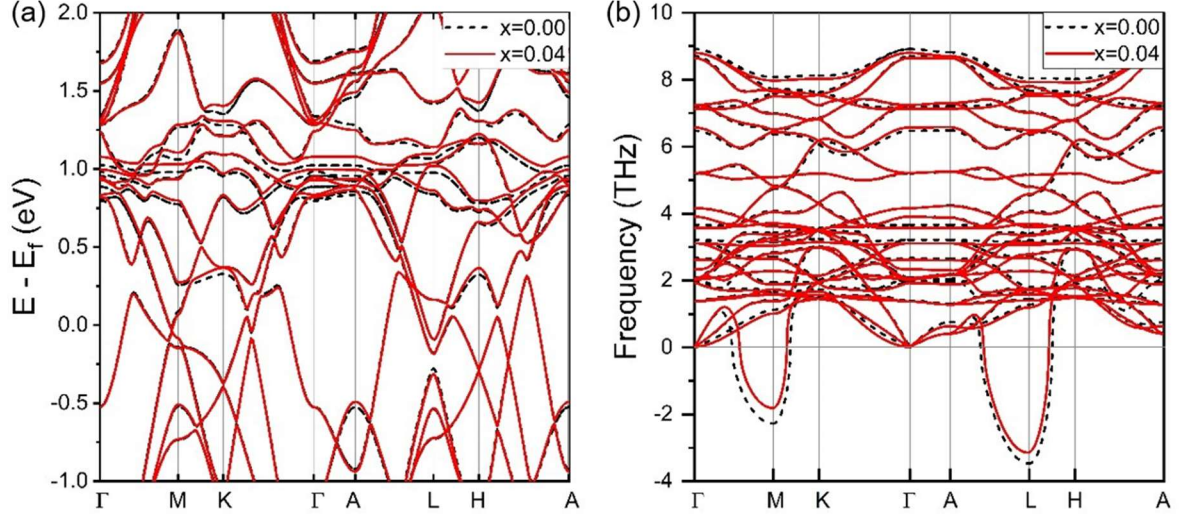


FIG. S5. (a) Calculated bands structures as different doping concentration of  $K(V_{1-x}Ta_x)_3Sb_5$ . (b) Calculated phonon spectrum, the Gaussian smearing is taken as  $\sigma = 0.05$ .

For calculations of the superconducting properties, we use the EPW code [39] which is interfaced with Quantum Espresso [40] and Wannier90 packages [41]. The energy cutoff of the plane-wave basis set is set at 80Ry. The Gaussian smearing method with a width of 0.004 Ry and a  $10 \times 10 \times 6$  k-mesh was employed for obtaining the ground-state electronic structure. The lattices of the pristine and doped structure from VASP relaxation are used. A  $10 \times 10 \times 6$  k-mesh and  $5 \times 5 \times 3$  q-mesh were adopted as coarse grids and the  $50 \times 50 \times 30$  k-mesh and  $25 \times 25 \times 15$  q-mesh were utilized as dense grids. After obtaining the Eliashberg spectral function [42]  $\alpha^2 F(\omega)$ , the superconducting transition temperature  $T_c$  was calculated with the Allen-Dynes formula [43],  $T_c = \frac{\omega_{log}}{1.2} \exp \left[ -1.04 \frac{1+\lambda}{\lambda - (0.62\lambda + 1)\mu^*} \right]$ , where  $\lambda = 2 \int \frac{d\omega}{\omega} \alpha^2 F(\omega)$  is the total electron-phonon-coupling strength, and  $\mu^*$  is the effective screened Coulomb repulsion constant, which is empirically [44,45] set to 0.16 and  $\omega_{log} = \exp \left[ \frac{2}{\lambda} \int \frac{d\omega}{\omega} \alpha^2 F(\omega) \ln(\omega) \right]$  is the logarithmic average of the Eliashberg spectral function. From Table S1 we can find that with doping 4% Ta to  $KV_3Sb_5$ , the superconducting transition temperature increases from 1.0K to 1.3K, which supports the enhanced superconductivity observed in experiments.

Doping	$T_c$ (K)	$\lambda$	$\omega_{log}$	$\Delta$ (meV)	$\mu^*$
0.00	1.013013	0.6352795	6.482754	0.153639	0.16
0.04	1.296265	0.6747295	6.553155	0.196598	0.16

Table S1. Calculated parameters for the Allen-Dynes formula.

The static generalized susceptibility of a system at wavevector  $\mathbf{q}$  in the random-phase-approximation (RPA) is written as:  $\hat{\chi}_{RPA}(\mathbf{q}) = \hat{\chi}^0(\mathbf{q}) \cdot [1 + U(\mathbf{q}) \cdot \hat{\chi}^0(\mathbf{q})]^{-1}$ , where  $\hat{\chi}^0(\mathbf{q})$  is the bare generalized susceptibility [46],  $U(\mathbf{q})$  is the on-site Kanamori-Hubbard interaction matrix [46]. The calculations are performed with Wannier tight-binding Hamiltonians, which are obtained by VASP2WANNIER90 interface [41]. 60 orbitals are considered including the  $p$  orbitals of K and  $d$  orbitals of V or Ta and spin degree of freedom. To find the effects of Ta doping on the Fermi surface instability, we calculated the generalized RPA susceptibility of  $K(V_{1-x}Ta_x)_3Sb_5$  at different doping concentrations, the results are shown in Fig. S6. For susceptibilities at the four

high-symmetry points, G, M, K and A, only at A and G points show diverging behaviors when increasing the value of the on-site Hubbard  $U$ . At the A point the susceptibilities host the largest diverging modes, see Fig. S6(a). Through careful analysis, we find that there are 3 leading diverging modes at  $U = 3.0\text{eV}$ , which turn out to be the 3 ferromagnetic orders with local magnetic moments along the  $x$ ,  $y$  and  $z$  axis, respectively, consistent with previous results [46]. Moreover, with increasing the doping of Ta, we can see in Fig. S6(b) that the divergences are getting weaker, which means that the doping of Ta will suppress the magnetic fluctuation. To this end, the Ta impurities are unlikely be magnetic. We further evaluate the nonmagnetic scattering potential of each Ta impurity. The central mass energy of local density of state for V atom and Ta atom is calculated to be  $0.177\text{eV}$  and  $0.056\text{eV}$ , respectively. Their difference estimates the scattering potential to be  $0.121\text{eV}$ , which is much smaller than the bandwidth on the order of  $1\text{eV}$ , based on which we evaluate the potential scattering is at the Born limit.

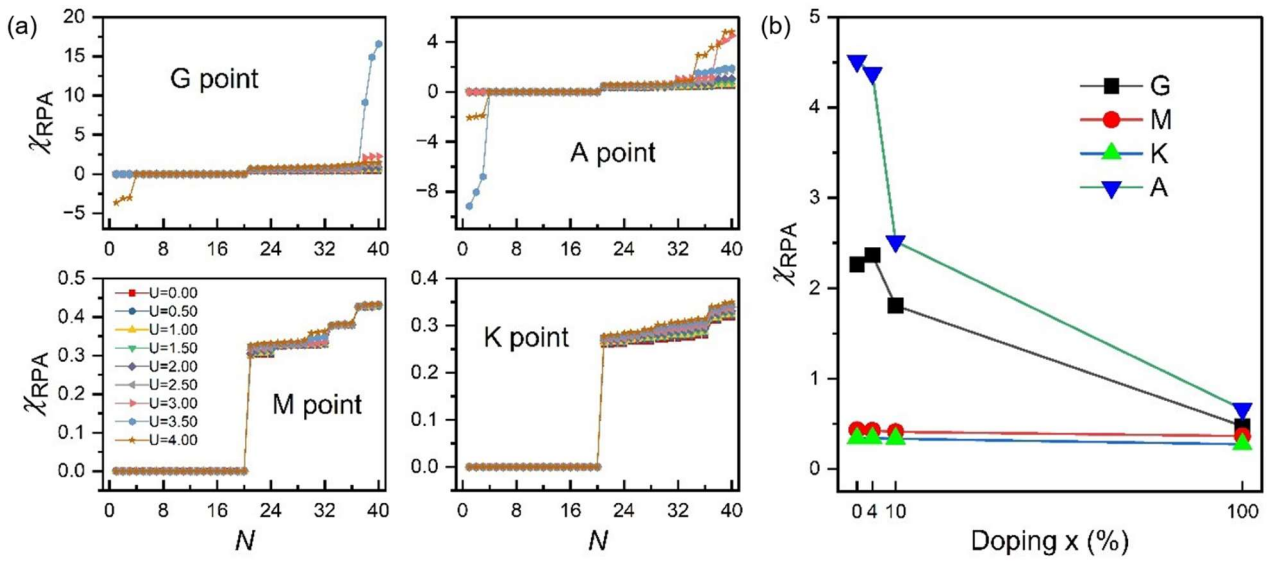


FIG. S6. (a) Calculated RPA susceptibilities at the high-symmetry points as a function of Hubbard on-site  $U$  with different doping. (b) Leading eigenvalues of the high-symmetry point as a function of doping.

## 6. Nonmagnetic PDW-breaking effect using Abrikosov-Gor'kov approach

We specifically focus on the disorder effect in the kagome PDW near the Born limit. Disorder will introduce a random fluctuation in the phase mode, which corresponds to the Goldstone mode arising from the translational symmetry broken. Thus, disorder is unfavorable to PDW states. Based on the minimum self-consistent model [16], we consider  $2 \times 2$  PDW in the kagome lattice associated with the V  $d$ -bands, in which the PDW state coexists with a charge order state. At the van Hove singularities, the Hamiltonian holding the intrinsic PDW states can be written as follows in the presence of the bond-attractive interactions:

$$\mathcal{H}_P = -J \sum_{\langle i,j \rangle, \sigma, \tau} (\sigma c_{i,\sigma}^\dagger c_{j,\sigma}^\dagger) (\tau c_{i,\bar{\tau}} c_{j,\tau}), \quad (2)$$

where  $\langle i,j \rangle$  are nearest bonds connecting sites  $i$  and  $j$ ,  $\sigma, \tau = -\bar{\sigma}, \bar{\tau} = \pm 1$ . In the mean-field approximation, non-vanishing  $\sum_{\tau} \langle \tau c_{i,\bar{\tau}} c_{j,\tau} \rangle$  indicates singlet pairing on bond  $\langle i,j \rangle$ .

In addition, a charge order state can be stabilized by including Coulomb repulsion on neighboring sites with the Hamiltonian form:

$$\mathcal{H}_V = V_1 \sum_{\langle i,j \rangle} n_i n_j + V_2 \sum_{\langle\langle i,j \rangle\rangle} n_i n_j. \quad (3)$$

These interactions can support chiral charge order states, and are compatible with (chiral) PDW states within the charge order state. Assuming that the disorder does not change the bare effective pairing interaction, the leading effect of disorder to suppress the PDW state, is due to the pair breaking effect, similar to that observed in ordinary superconducting states. In order to see the disorder effect clearly, we utilize the Abrikosov-Gor'kov formula [47-49], with the vertex correction up to the Born approximation, as follows:

$$\ln \frac{T_c}{\tilde{T}_c} = \chi \left[ \psi \left( \frac{1}{2} + x \right) - \psi \left( \frac{1}{2} \right) \right], \quad (4)$$

where  $\psi$  is the digamma function, and  $\chi = \left\langle \left| \Gamma^l(k, q) \right|^2 \right\rangle_{\text{FS}} - \left| \langle \Gamma^l(k) \rangle_{\text{FS}} \right|^2$  measures the inhomogeneity of the gap function on the Fermi surface.

Our Abrikosov-Gor'kov analysis will be based on the gap function, which is highly anisotropic for the PDW state [16]. For simplicity, the gap function can be fitted through the following model function:

$$\Delta(\mathbf{k}) = \Delta_0^\alpha \exp(2i\theta_{\mathbf{k}}) + \sum_{\theta_p} \Delta_0 \exp(2i\theta_{\mathbf{k}}) \left[ e^{-\frac{(\theta_{\mathbf{k}} - \theta_p + \delta\theta)^2}{2\Delta\theta^2}} + e^{-\frac{(\theta_{\mathbf{k}} - \theta_p - \delta\theta)^2}{2\Delta\theta^2}} \right] \quad (5)$$

where  $\theta_{\mathbf{k}}$  is the angular position of the momentum  $\mathbf{k}$  on the Fermi surface,  $\Delta_0$  is the amplitude of pairing. In our model function, the double-peak feature is fitted by the Gaussian function located at  $\theta_p = 2\pi p / 6, p = 0, 1, \dots, 5$  split by  $\pm\delta\theta$  and of width  $\Delta\theta$ . Moreover, the minigap is included with a power-law suppressed amplitude  $\Delta\theta$ . Specifically, the parameters here are:  $\Delta_0 = 0.03$ ,  $\delta\theta = 0.0375\pi$ ,  $\Delta\theta = 0.0125\pi$ , and  $\alpha = 3$ . Such complex gap function in momentum space mainly results from the phase sign modulation of the PDW in real space [16].

With the relationship shown in Eq. (4), we discuss the disorder effect case by case. First, we consider the isotropic s-wave pairing. Now  $\chi = 0$ , thus  $\tilde{T}_c = T_c$ , that is, isotropic s wave pairing is robust against nonmagnetic disorders, which is known as Anderson theorem. Next, we focus on the PDW states as mentioned above. By normalizing the gap function as  $\Delta(\mathbf{k}) = \tilde{\Delta}_0 \Gamma(k)$  with  $\left\langle \left| \Gamma^l(k, q) \right|^2 \right\rangle_{\text{FS}} = 1$ , and calculating  $\chi = \left\langle \left| \Gamma^l(k, q) \right|^2 \right\rangle_{\text{FS}} - \left| \langle \Gamma^l(k) \rangle_{\text{FS}} \right|^2$ , then we obtain the suppression of  $T_c$  due to disorder for the kagome PDW, as shown by the blue curve in Fig. S7. The red line confirms Anderson's theorem on s-wave pairing, while the blue line illustrates the suppression of PDW. These results can be generalized to a phenomenological model considering  $p$ - $d$  PDW order [6]. Such nonmagnetic PDW breaking effect is similarly supported by calculations by self-consistent real-space Bogoliubov-de-Gennes equations, which will be published elsewhere.

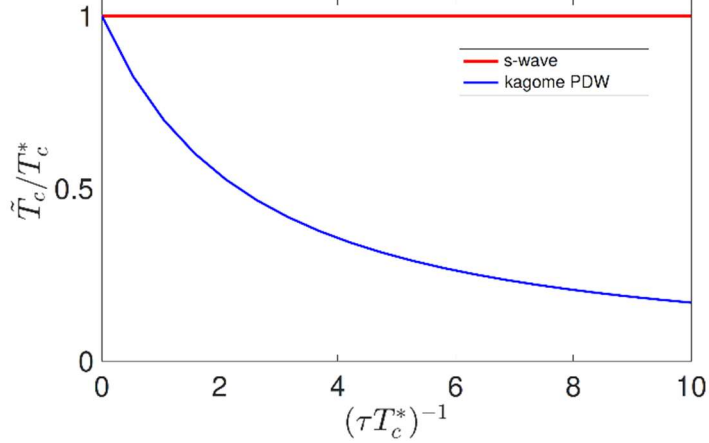


FIG. S7. Nonmagnetic PDW breaking effect using Abrikosov-Gor'kov approach.

### 7. Ginzburg-Landau analysis for competing superconducting instabilities

To understand the enhanced uniform superconductivity and multi-orbital nature of the electron pairing, we further perform a Ginzburg-Landau analysis. From the experimental evidence in our and related studies, the dominant symmetry-broken phases in the system are: 1) a high temperature  $2 \times 2$  charge order  $\Delta_{\text{CO}}(\mathbf{M}_i)$ , and 2) a phonon driven  $s$ -wave superconducting order  $\Delta_p(\Gamma)$  on the Sb  $p_z$ -orbital-derived central circular pocket. As the temperature is reduced, V  $d$ -orbital derived hexagonal pocket develops superconducting pairing with two kinds: 3) a proximity-induced superconducting order on the  $d$ -orbital pockets, which could be of conventional  $s$ -wave type or feature a  $d+id$  wave gap structure in accordance with predictions from an intrinsically electronic pairing mechanism [50,51]  $\Delta_d(\Gamma)$ . However, only the former one can couple to the dominant superconducting order  $\Delta_p(\Gamma)$  (Ref. 46). Hence, we will focus on  $s$ -wave pairing on the  $d$ -orbital state in the following. 4) A PDW state, which arises from an inter-pocket pairing between the  $p$ - and  $d$ -pockets  $\Delta_{pd}(\mathbf{M}_i)$ . This order requires a finite momentum condensate, which is commensurate with the charge order. Therefore, we have four different instabilities with corresponding transition temperatures  $T^* \gg T_p > T_{d/pd}$ .

Next, we expand the free energy in the Ginzburg-Landau formalism. Since the charge order transition scale is separated from the subsequent superconducting transitions, we do not treat the charge order as a Ginzburg-Landau parameter but incorporate its effects into the symmetry requirements for the free energy functional. In the charge order state, the system exhibits reduced translational symmetry, so all  $M_i$  are mapped back to the  $\Gamma$  point. Consequently, we drop the momentum label in the superconducting order parameter and treat them all as ordinary superconducting instabilities. The nature of the PDW phase is thereby encoded in the inter-orbital character of its Cooper pairs.

In the Ginzburg-Landau analysis, the symmetry of the PDW state is highly sensitive to the precise form of the parent charge order parameter [16,17]. However, the nature of the charge-ordered state is still under discussions [52-61]. Rather than restricting our analysis to a specific charge order state, we implicitly assume, that the PDW state will transform within an irreducible representation of the enlarged point group  $C_{6v}'''$ , compatible with the coupling to the irreducible content of the charge order phase. Consequently, we will not explicate all fourth-order terms in the Ginzburg-Landau formalism that would determine the energetically favorable linear combination of multi-dimensional irreducible representations, but instead represent them in a single Ginzburg-Landau coefficient  $\beta_i$ . For a detailed discussion on the coupling of the different orders on the V sites, we refer to Ref. 46.

To each superconducting order parameter  $\Delta_i$ , we assign an intrinsic transition temperature  $T_c^i$ , which contributes to the Ginzburg-Landau functional

$$F_i = \alpha_i |\Delta_i|^2 + \beta_i |\Delta_i|^4 + \mathcal{O}(\Delta_i^6). \quad (6)$$

Near  $T_c^i$  the second-order coefficient scales as  $\alpha_i \sim \tilde{\alpha}_i (T - T_c^i)$  and  $\beta$  is temperature-independent. Since all  $T_c^i$  are expected to be sufficiently close, this approximation is valid for investigating the mutual coupling of the SC orders. The full Ginzburg-Landau functional, up to fourth order, is then written as:

$$\begin{aligned} F = & \alpha_p |\Delta_p|^2 + \alpha_d |\Delta_d|^2 + \alpha_{dp} |\Delta_{dp}|^2 \\ & + a_{01} (\Delta_p \Delta_d^* + h.c.) + a_{02} (\Delta_p \Delta_{pd}^* + h.c.) + a_{12} (\Delta_d \Delta_{pd}^* + h.c.) \\ & + \beta p |\Delta_p|^4 + \beta d |\Delta_d|^4 + \beta dp |\Delta_{dp}|^4 \\ & + b_{01} (\Delta_p^2 (\Delta_d^*)^2 + h.c.) + b_{02} (\Delta_p^2 (\Delta_{pd}^*)^2 + h.c.) + b_{12} (\Delta_d^2 (\Delta_{pd}^*)^2 + h.c.) \\ & + b_{012} (\Delta_p \Delta_d^* |\Delta_{pd}|^2 + h.c.) + b_{201} (\Delta_{pd} \Delta_p^* |\Delta_d|^2 + h.c.) \\ & + b_{120} (\Delta_d \Delta_{pd}^* |\Delta_p|^2 + h.c.) + \mathcal{O}(\Delta_i^6). \end{aligned} \quad (7)$$

The additional second-order terms arise from the coupling between different order parameters. The presence of  $a_{02}$ ,  $a_{12} \propto \Delta_{CO}$  is a direct result of the underlying charge order phase, as it stems from the band-folding inside the reduced Brillouin zone of the  $2 \times 2$  state. The actual superconducting transition temperature is determined as the temperature at which the second-order coefficient matrix becomes singular, *i.e.*

$$\det \begin{pmatrix} \alpha_p & a_{01} & a_{02} \\ a_{01} & \alpha_d & a_{12} \\ a_{02} & a_{12} & \alpha_{pd} \end{pmatrix} = 0. \quad (8)$$

Since the coupling between the order parameters is already captured by the second-order terms, which are dominant near the phase transition, we focus on these terms and disregard the fourth-order terms in the following analysis.

In the pristine case, the resulting superconducting phase on the  $d$ -pocket is exclusively governed by  $\Delta_{pd}$ , leading to a partially gapped Fermi surface with residual Fermi arcs [6,7]. This can be understood within the Ginzburg-Landau picture: The second-order coefficients in Eq. (7) are determined by the overlaps between the different SC orders with the bare particle-particle kernel

$$a_{ij} = \sum_{\{o_i\} \mathbf{k}} \int d\tau \left\langle \Delta_i^{o_1 o_2}(\mathbf{k}) | G_{o_1 o_3}(\mathbf{k}, \tau) G_{o_2 o_4}(-\mathbf{k}, \tau) | \Delta_j^{o_3 o_4}(\mathbf{k}) \right\rangle. \quad (9)$$

where  $G_{o_1 o_2}(\mathbf{k}, \tau)$  is the single-particle Green's function in the charge-ordered phase. For all possible coupling terms, the Green's functions only contribute non-zero terms at the intersection of the backfolded pockets, where both  $\Delta_{pd}$  and  $\Delta_d$  can be of comparable size. While  $\Delta_d$  may also exhibit a finite gap away from the band crossings to gain condensation energy, *i.e.*  $T_c^d > T_c^{pd}$ , the orbital structure of the gap functions suggests  $a_{02} > a_{01}$  due to the more favorable orbital overlap between the superconducting states. With  $T_c^p \gg T_c^d$ ,  $T_c^{pd}$ , the competition of these two effects determines the superconducting ground state. In the pristine case, the effect of  $a_{02}$  seems to dominate over the intrinsic transition temperature difference.

In the system with randomly distributed Ta dopants, two striking effects can be observed: i) the  $d$ -orbital pockets are substantially gapped, reducing the remaining density of states within the superconducting gap; ii) the superconducting transition temperature is substantially enhanced compared to the pristine case. Since the

suppression of the charge order is marginal and observed at a temperature well above the superconducting transition, we do not account for changes in the charge order-mediated coupling in the Ginzburg-Landau functional of Eq. (7). It is known that disorder can lead to an enhancement of  $T_c$  if impurities alter the density of states distribution in a way that increases the condensation energy [62]. We incorporate the effect of disorder into our phenomenological theory by accounting for its influence on the second-order coefficients. While the s-wave superconducting orders  $\Delta_p$  and  $\Delta_d$  are robust against non-magnetic impurities,  $\Delta_{pd}$  suffers from a strong suppression of  $T_c$  in the presence of disorder (as evidenced by the Abrikosov-Gor'kov calculations). We note that the composite  $pd$ -nature of the superconducting state is crucial: it has been shown that the sublattice polarization on the  $d$ -orbital derived Fermi surface protects also unconventional superconducting orders from local disorder [63]. However, disorder destroys the phase coherence of the inter-pocket Cooper pairs, leading to a substantial decrease of  $T_c^{pd}$ . We mimic this effect in Eq. (8) by decreasing  $T_c^{pd}$  and simultaneously increase  $T_c^p$  to account for the enhanced electron phonon coupling for conventional pairing potential on the Sb  $p$ -orbital derived pocket. Additionally, impurities significantly increase the inter-pocket scattering [64], which we incorporate by a change of  $a_{01}$  while keeping the other parameters constant. Fig. S8 shows the qualitative evolution of the gap structure as a function of the varied parameter. We observe a crossover from  $\Delta_{pd}$  to  $\Delta_d$  descendant superconducting instability on the  $d$ -orbital pocket, which coincides with quasi-particle interference measurements. Similarly, the overall superconductivity is enhanced for a sufficiently large inter-pocket coupling beyond the increase from the electron phonon coupling incorporated in the Ginzburg-Landau parameter: it exceeds the increase of  $T_c^p$  by a factor of 2 for the chosen parameters.

While our phenomenological Ginzburg-Landau theory does not allow for a quantitative estimate of the  $T_c$  enhancement due to Ta dopants, it clearly showcases that the multi-orbital and multi-pocket nature with different competing and cooperating superconducting orders in the non-trivial Fermi surface topology allows to considerably enhance  $T_c$  beyond the 30% increase predicted by conventional intra-pocket s-wave pairing mechanism.

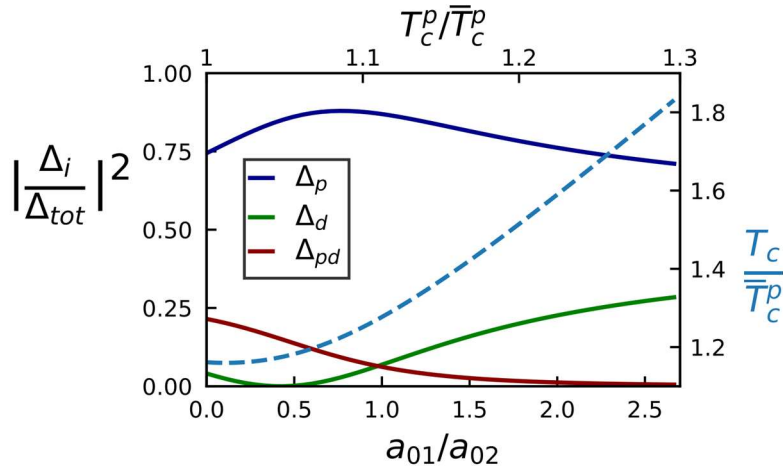


FIG. S8. Schematic temperature evolution upon introduction of non-magnetic impurities. We have used  $\alpha_d = \alpha_{pd} = 0.8\alpha_p$  and fixed  $T_c^d = 0.3$  and  $a_{02} = a_{12} = 0.3$ . The effect of Ta dopants is mimicked by a 30% increase of  $T_c^p$  compared to the pristine value  $\bar{T}_c^p = 1$  as indicated by the electron-phonon coupling calculations. The simultaneous suppression of  $T_c^{pd}$  due to nonmagnetic PDW breaking effect is modelled by

$T_c^{pd}=0.3(2-T_c^p/\bar{T}_c^p)$ . The qualitative behavior of the gap and  $T_C$  evolution is independent of the chosen parameters. Only the crossover between  $\Delta_{pd}$  and  $\Delta_d$  dominated regimes is slightly shifted.

## References

- [33] Z. Huang *et al.*, *Sci. Bull.* **69**, 885 (2024).
- [34] G. Kresse and J. Furthmüller, *Phys. Rev. B* **54**, 11169 (1996).
- [35] J. P. Perdew, K. Burke, and M. Ernzerhof, *Phys. Rev. Lett.* **78**, 1396 (1997).
- [36] L. Bellaïche and D. Vanderbilt, *Phys. Rev. B* **61**, 7877 (2000).
- [37] A. Togo, L. Chaput, T. Tadano, and I. Tanaka, *J. Phys.: Condens. Matter* **35**, 353001 (2023).
- [38] A. Carreras, A. Togo, and I. Tanaka, *Comput. Phys. Commun.* **221**, 221 (2017).
- [39] J. Noffsinger, F. Giustino, B. D. Malone, C.-H. Park, S. G. Louie, and M. L. Cohen, *Comput. Phys. Commun.* **181**, 2140 (2010).
- [40] P. Giannozzi *et al.*, *J. Phys.: Condens. Matter* **21**, 395502 (2009).
- [41] A. A. Mostofi, J. R. Yates, G. Pizzi, Y.-S. Lee, I. Souza, D. Vanderbilt, and N. Marzari, *Comput. Phys. Commun.* **185**, 2309 (2014).
- [42] E. R. Margine and F. Giustino, *Phys. Rev. B* **87**, 024505 (2013).
- [43] P. B. Allen, *Phys. Rev. B* **6**, 2577 (1972).
- [44] C. F. Richardson and N. W. Ashcroft, *Phys. Rev. Lett.* **78**, 118 (1997).
- [45] K.-H. Lee, K. J. Chang, and M. L. Cohen, *Phys. Rev. B* **52**, 1425 (1995).
- [46] H.-Y. Ma, J.-X. Yin, M. Zahid Hasan, and J. Liu, *Phys. Rev. B* **106**, 155125 (2022).
- [47] A. A. Abrikosov and L. P. Gor'kov, *Zhur. Eksptl'. i Teoret. Fiz.* **39**, 1781 (1960).
- [48] A. Abrikosov, *Physica C: Superconductivity* **214**, 107 (1993).
- [49] P. Hohenberg, *Sov. Phys. JETP* **18**, 834 (1964).
- [50] T. Schwemmer *et al.*, *Phys. Rev. B* **110**, 024501 (2024).
- [51] J. B. Profe, L. Klebl, F. Grandi, H. Hohmann, M. Dürrnagel, T. Schwemmer, R. Thomale, and D. M. Kennes, *Phys. Rev. Res.* **6**, 043078 (2024).
- [52] T. Neupert, M. M. Denner, J.-X. Yin, R. Thomale, and M. Z. Hasan, *Nat. Phys.* **18**, 137 (2022).
- [53] H. Tan, Y. Liu, Z. Wang, and B. Yan, *Phys. Rev. Lett.* **127**, 046401 (2021).
- [54] X. Feng, K. Jiang, Z. Wang, and J. Hu, *Sci. Bull.* **66**, 1384 (2021).
- [55] Y.-P. Lin and R. M. Nandkishore, *Phys. Rev. B* **104** (2021).
- [56] T. Park, M. Ye, and L. Balents, *Phys. Rev. B* **104**, 035142 (2021).
- [57] M. H. Christensen, T. Birol, B. M. Andersen, and R. M. Fernandes, *Phys. Rev. B* **106**, 144504 (2022).
- [58] R. Tazai, Y. Yamakawa, and H. Kontani, *Nat. Commun.* **14**, 7845 (2023).
- [59] J.-W. Dong, Z. Wang, and S. Zhou, *Phys. Rev. B* **107**, 045127 (2023).
- [60] N. Mohanta, *Phys. Rev. B* **108**, L220507 (2023).
- [61] R.-Q. Fu, J. Zhan, M. Dürrnagel, H. Hohmann, R. Thomale, J. Hu, Z. Wang, S. Zhou, and X. Wu, Preprint at arXiv:2405.09451 (2024).
- [62] M. N. Gastiasoro and B. M. Andersen, *Phys. Rev. B* **98**, 184510 (2018).
- [63] S. C. Holbæk, M. H. Christensen, A. Kreisel, and B. M. Andersen, *Phys. Rev. B* **108**, 144508 (2023).
- [64] A. A. Golubov and I. I. Mazin, *Phys. Rev. B* **55**, 15146 (1997).